The effect of material cyclic deformation properties on residual stress generation by laser shock processing

Angulo, I., Cordovilla, F., García-Beltrán, A., Smyth, N. S., Langer, K., Fitzpatrick, M. E. & Ocaña, J. L.

Original citation & hyperlink:
Angulo, I, Cordovilla, F, García-Beltrán, A, Smyth, NS, Langer, K, Fitzpatrick, ME & Ocaña, JL 2019, 'The effect of material cyclic deformation properties on residual stress generation by laser shock processing', International Journal of Mechanical Sciences, vol. 156, pp. 370-381.
https://dx.doi.org/10.1016/j.ijmecsci.2019.03.029

DOI 10.1016/j.ijmecsci.2019.03.029
ISSN 0020-7403

Publisher: Elsevier

The effect of material cyclic deformation properties on residual stress generation by laser shock processing

I. Angulo[1], F. Cordovilla[1], A. García-Beltrán[1], N.S. Smyth[2], K. Langer[3], M.E. Fitzpatrick[2], J.L. Ocaña[1]

[1] UPM Laser Centre. ETS Ingenieros Industriales. Polytechnical University of Madrid.
C/ José Gutiérrez Abascal, 2. 28006 Madrid. SPAIN
[2] Centre for Manufacturing and Materials Engineering, Coventry University.
Priory St, Coventry CV1 5FB, UK
[3] Air Force Research Laboratory, AFRL/RQVS, Wright-Patterson Air Force Base, OH 45433, USA

Abstract

Laser shock processing (LSP) is a mechanical surface treatment to induce a compressive residual stress state into the near surface region of a metallic component. The effect of the cyclic deformation properties of ductile materials on the final residual stress fields obtained by LSP is analysed. Conventional modelling approaches either use simple tensile yield criteria, or isotropic hardening models if cyclic straining response is considered for the material during the peen processing. In LSP, the material is likely to be subject to cyclic loading because of reverse yielding after the initial plastic deformation. The combination of experiment and modelling shows that the incorporation of experimentally-determined cyclic stress-strain data, including mechanical hysteresis, into material deformation models is required to correctly reflect the cyclic deformation processes during LSP treatment and obtain accurate predictions of the induced residual stresses.

Keywords: Laser shock processing; Cyclic hardening; Residual stress; Shock waves; Finite element analysis.

1. Introduction

Laser shock processing (LSP, also called laser shock peening or just laser peening) is a mechanical surface treatment that uses a high intensity pulsed laser beam to induce a compressive residual stress state into the near surface region of a metallic component. This treatment has been successfully implemented in the design of high-added-value engineering applications (for instance biomedical implants) [1]. An accurate design of the process, concerning the prediction of the final residual stress distribution, leads to an increase in the fatigue life which has been widely documented by several authors [2-4].

During LSP, the laser energy forces a sudden vaporization of the target surface into a high temperature and density plasma, which immediately induces a shock wave that propagates into the material. When the magnitude of the plasma pressure exceeds the Hugoniot elastic limit of the material, near-surface plasticity is presented. The compensatory elastic springback of the surrounding material then induces a largely in-plane (transverse to the wave propagation direction) residual stress. Numerical modelling provides the fundamental to correlate the behaviour of the material with the suitable parameters to design a process leading to an optimal residual stress state.

In computational mechanics simulation, LSP is often modelled using the assumption of isotropic hardening (*i.e.*, the Johnson-Cook model [5]). However, in practice, the relaxation of the elastically-stressed material below the plastically deformed layer often causes reverse yielding. This unload cycle is therefore expected to partially develop in a yield surface displacement that cannot be modelled by isotropic hardening.

Isotropic hardening predicts an increase in the yield surface size for both tensile and compressive deformation. Once the material is deformed plastically with the application of a tensile (or compressive) load, compressive (or tensile) stresses of the same magnitude will not result in yield of the material [6]. In contrast, kinematic hardening models assume that the size (and sometimes the shape) of the yield surface remains unchanged under additional load, but that the position of the yield surface translates in stress space.

For cyclic deformation in which tensile and compressive cycles alternate, such as the loading-unloading experienced by a material during LSP, an accurate representation of the plasticity response will typically be a combination of these two extremes. According to experimental results [7], after a plastic tensile load, lower magnitude compressive stresses can result in plastic deformation. This is known as the Bauschinger effect. For the material modelling of this effect, it is necessary to consider kinematic hardening. The first kinematic hardening rule was proposed by Prager [8]. It represents properly the Bauschinger effect when symmetric compressive-tensile cycles are applied. However, this model does not predict the cumulative plastic strain for asymmetric cycles known as the ratcheting effect. Based on linear kinematic hardening, some modifications of Prager's rule were introduced [9-13]. However, the ratcheting effect is not predicted by these updated models.

In order to predict it, a nonlinear hardening model was introduced by Armstrong and Frederick [14]. Chaboche [15] decomposed the back-stress into multiple components with different convergence rates which led to a better approach to the ratcheting behaviour of a material subject to a wider range of stresses and strains. Chaboche [16], in a similar way as Ohno and Wang [17], used later a modification of the original Armstrong-Frederick model. Finally, in order to account for the multiaxial ratcheting problem, several models have been developed since then based on the Armstrong nonlinear model [18-24].

On this basis, it can be concluded that an isotropic hardening model is only valid for processes in which the material yields only in tension or only in compression. For the case of alternating tensile-compressive (or compressive-tensile) cycles, the evolution of the yield stress needs to be reflected with the aid of a combined hardening model. These models include a kinematic hardening law and an isotropic hardening one, which predict the evolution of the yield surface displacement and the yield surface size, respectively.

In this paper, the explicit consideration of the cyclic plasticity phenomenon to predict residual stresses as a consequence of the LSP treatment is analysed. Firstly, an isotropic hardening model was calibrated using monotonic stress-strain curves of Al 2624 T39 and Al 2624 T351 [7]. The inappropriateness of this model to predict cyclic behaviour is shown in section 2.2.1: A clear overestimation is predicted after several cycles. In consequence, a combined hardening model was calibrated considering the cyclic response of both alloys obtained experimentally by the authors [7]. Taking into account that the physics of the cyclic plasticity are inherent to LSP, the implemented combined hardening model is therefore expected to predict more precise results in LSP treatments.

The calibrated combined model was then used for the numerical simulation of LSP processes, with clear differences found with respect to the results based on isotropic (*i.e.*, Johnson-Cook) models. In addition, based on the evolution of the shockwave pressure as it propagates through the material, the range of affected depths of the material in which the cyclic behaviour is present has been identified as a key feature for the practical prediction of the resulting residual stresses fields in the LSP-treated material. Overall, the explicit consideration of the cyclic behaviour leads to an improvement of the modelling accuracy of LSP processes, finally applicable to an improved predictive design capability.

2. Theoretical background

2.1. Elastic and Plastic Deformations in the Shock Compression of Metallic Materials

In processes where high pressures are applied to a material, depending on the impulse time and the geometry of the affected surface, uniaxial stress or uniaxial strain behaviour can be induced. Once the pressure is applied, a transverse wave starts to propagate on the surface plane. If the pressure pulse duration is negligible compared with the time needed for the transverse wave to reach the limit of the surface, the material is said to experience uniaxial strain behaviour widely analysed by Ballard [25]. In the opposite case, the material would experience uniaxial stress behaviour. For typical LSP processes, with pressure pulses on the order of nanoseconds [26-28], the material is considered to be subject to uniaxial strain loading conditions.

The von Mises stress in its general form is presented in equation 1a, where σ_1, σ_2 and σ_3 are the principal stresses. In uniaxial strain behaviour, where axial symmetry exists, two of the three principal stresses are parallel to material´s surface and both have the same magnitude ($\sigma_1 = \sigma_2 = \sigma_r$). The third one is then collinear with the wave propagation direction, σ_3, which is denoted as σ_z using the notation of axial-symmetrical states. Therefore, the von Mises criterion reduces to equation 1b. The material is deformed plastically when $\sigma_v = \sigma_y$, where σ_y is the yield stress. In addition, the stress and strain tensors follow the mechanical laws given by equation 2.

$$\sigma_v = \sqrt{\frac{(\sigma_1 - \sigma_2)^2 + (\sigma_3 - \sigma_1)^2 + (\sigma_2 - \sigma_3)^2}{2}} \tag{1a}$$

$$\sigma_v = |\sigma_z - \sigma_r| \tag{1b}$$

$$\bar{\sigma} = \begin{pmatrix} \sigma_r & 0 & 0 \\ 0 & \sigma_r & 0 \\ 0 & 0 & \sigma_z \end{pmatrix} \qquad \bar{\varepsilon} = \begin{pmatrix} 0 & 0 & 0 \\ 0 & 0 & 0 \\ 0 & 0 & \varepsilon_{ez} \end{pmatrix} \qquad \overline{\varepsilon_p} = \begin{pmatrix} -\varepsilon_{pz}/2 & 0 & 0 \\ 0 & -\varepsilon_{pz}/2 & 0 \\ 0 & 0 & \varepsilon_{pz} \end{pmatrix} \tag{2}$$

where:

σ_r ≡ Stress in the transverse direction.

σ_z ≡ Stress in the axial direction.

ε_{ez} ≡ Elastic strain in the axial direction.

ε_{pz} ≡ Plastic strain in the axial direction.

Using the generalized Hooke's formula (equations 3 and 4), which represents the material's elasto-plastic behaviour, purely elastic behaviour is obtained and defined by equations 5 and 6.

$$\sigma_r = \frac{\nu}{(1+\nu)(1-2\nu)} E\varepsilon_{ez} + \frac{1}{2(1+\nu)} E\varepsilon_{pz} \tag{3}$$

$$\sigma_z = \frac{\nu}{(1+\nu)(1-2\nu)} E\varepsilon_{ez} + \frac{1}{1+\nu} E\varepsilon_{ez} - \frac{1}{1+\nu} E\varepsilon_{pz} \tag{4}$$

Under purely elastic behaviour:

$$\sigma_r = \frac{\nu}{(1+\nu)(1-2\nu)} E\varepsilon_{ez} \tag{5}$$

$$\sigma_z = \frac{1-\nu}{(1+\nu)(1-2\nu)} E\varepsilon_{ez} \tag{6}$$

Where:

E ≡ Young modulus.

ν ≡ Poisson´s ratio.

The expression for the Hugoniot elastic limit (σ_H), which is defined as the yield stress of a material subject to uniaxial strain loading conditions, is:

$$\sigma_H = \frac{1-\nu}{1-2\nu}\sigma_y \tag{7}$$

Considering an elastic-perfectly plastic model (assumed to properly represent the behaviour of the studied materials), the respective evolution in the $(\sigma_z, \varepsilon_{pz})$ and (σ_z, σ_r) planes of the axial stress in a typical LSP stress-release cycle for an applied pressure $P_{MAX} > 2\sigma_H$ are represented in figures 1 and 2. From these figures, it can be concluded that [25]:

(a)	If $(P_{MAX} < \sigma_H)$	Only elastic deformation occurs.
(b)	If $(\sigma_H < P_{MAX} < 2\sigma_H)$	Plastic strain occurs with purely elastic reverse strain.
(c)	If $(P_{MAX} > 2\sigma_H)$	The material develops plastic strain during the load cycle ($\varepsilon_{pz\ load}$) and unload cycle ($\varepsilon_{pz\ unload}$), which are defined respectively by equations 8 and 9. The residual plastic strain is obtained by subtracting ($\varepsilon_{pz\ unload}$) from ($\varepsilon_{pz\ load}$) (eq 10).

where:

P_{MAX} ≡ Maximum applied pressure

$$\varepsilon_{pz\ load} = \frac{2(1-2\nu)}{E}(P_{MAX} - \sigma_H) \tag{8}$$

$$\varepsilon_{pz\ unload} = \frac{2(1-2\nu)}{E}(P_{MAX} - 2\sigma_H) \tag{9}$$

$$\varepsilon_{pz\ res} = \left(\frac{1-2\nu}{E}\right)2\sigma_H \tag{10}$$

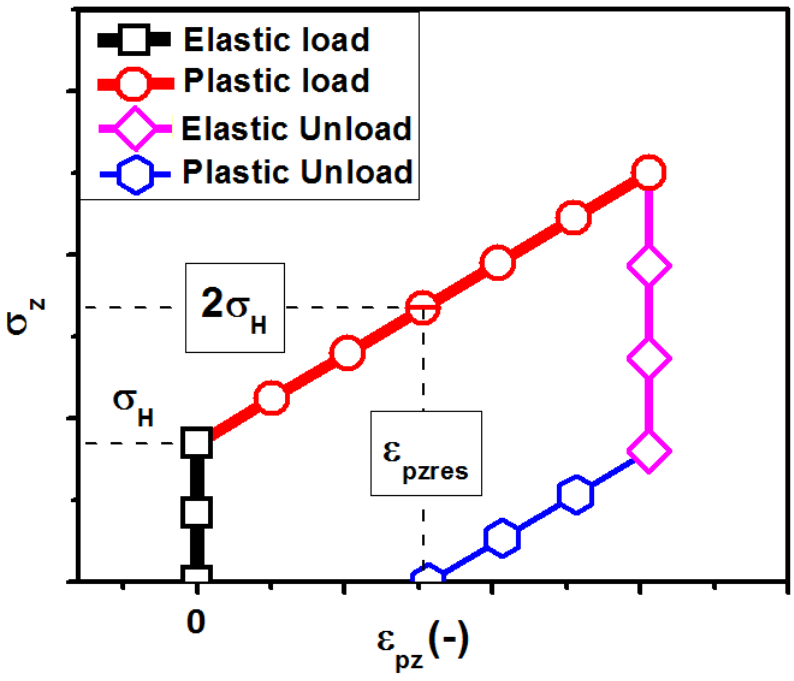

Figure 1: σ_z-ε_{pz} diagram for $P_{MAX}>2\sigma_H$.

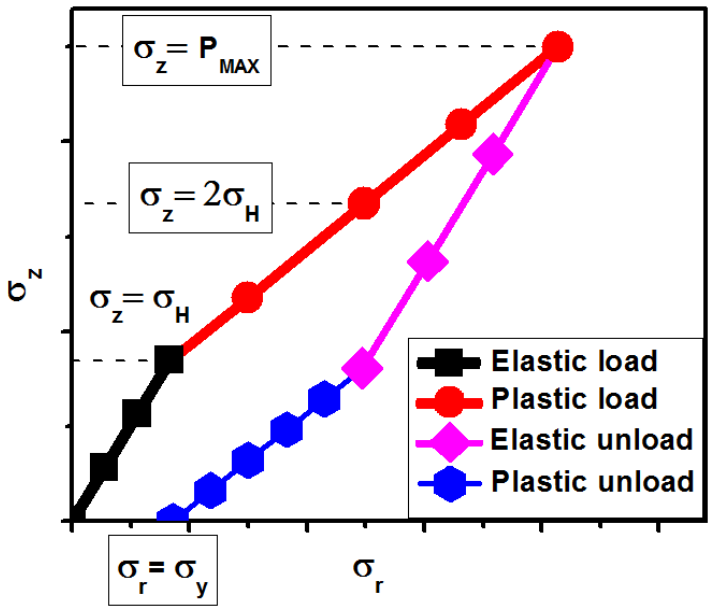

Figure 2: σ_z- σ_r diagram for $P_{MAX}>2\sigma_H$.

As an important result, although the target material only experiences loading in one direction, when the peak pressure pulse dissipates, the material undergoes an unload cycle as a consequence of elastic relaxation, which is sufficient to cause plasticity in the opposite direction. Hence the phenomenon of cyclic plasticity has been identified as a relevant issue, especially for those regions near-surface where the plastic recovery is non-negligible compared with the initial plastic deformation. Concretely, if the applied maximum pressure is lower than $2\sigma_H$, no cyclic hardening is experienced by the material and both isotropic and combined models predict approximately the same results. On the contrary, if the applied maximum pressure exceeds $2\sigma_H$, cyclic deformation takes place, with the plastic strain bounded by $\varepsilon_{pz\,res}$. In section 3.2, a criterion to identify approximately the critical depth to which the cyclic behaviour extends is presented.

2.2. Definition of a Model for the Explicit Consideration of Cyclic Deformation Properties

In order to proceed with the practical estimation of the differences of both types of material hardening models (isotropic and combined), the experimental results of the monotonic and cyclic behaviour of two ductile materials (Al2624 in the T39 and T351 tempers) obtained by Zabeen *et al.* [7] have been considered. These cyclic tests were carried out in strain-control, with the material cycled up to 7 cycles with a maximum strain of ±2%. Figure 3 shows the results: while Al 2624 T39 reaches a saturation value after four cycles, Al 2624 T351 gradually hardens up to the seventh cycle.

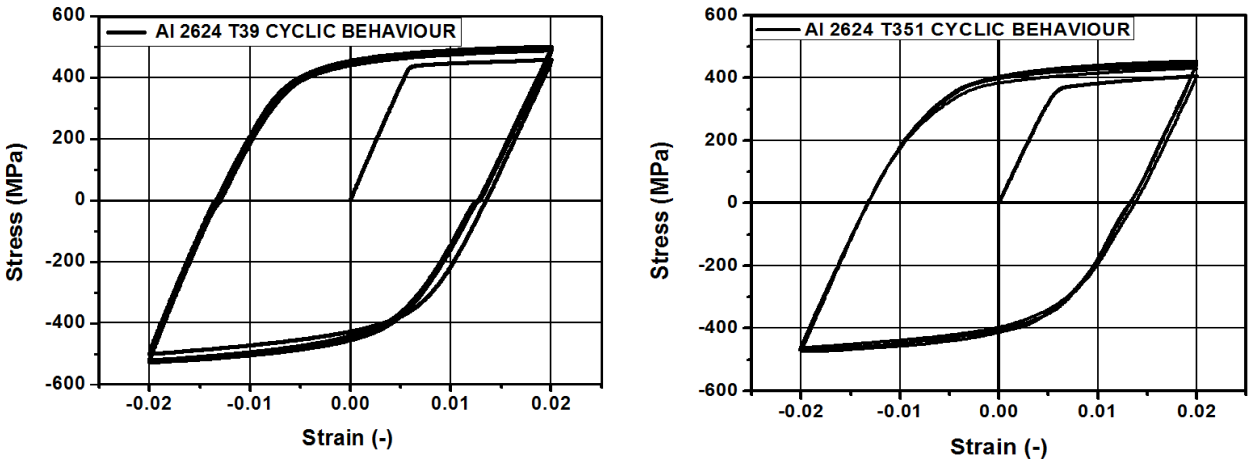

Figure 3: Experimental results of strain-control cycles up to 7 cycles with a maximum strain of ±2%. T39 (left), T351 (right).

With the aid of the experimental monotonic stress-strain curves [7], and experimental cyclic ones presented in figure 3, an isotropic model and a combined model have been calibrated. In the case of the isotropic model, the experimental monotonic stress-strain curves have been used for the calibration. Additionally, the cyclic behaviour of the material has been taken into account in order to model the yield surface displacement in the combined hardening model.

2.2.1 Exponential isotropic hardening model

In this section, an exponential isotropic hardening model is calibrated for both materials. The considered isotropic model is defined by equation 11 and requires three calibration parameters: (σ_0, K and n). The purpose of selecting this isotropic exponential yield function is that it is widely used to model LSP processes, highlighting its limitations when multiple cycles are applied.

$$\sigma_y = \sigma_0 + K{\varepsilon_p}^n \tag{11}$$

where σ_y is the yield stress, σ_0 is the first yield stress, and K and n are constants to be calibrated

A least square method has been used to calibrate σ_0, K and n (table 1) considering the experimental monotonic stress-strain curves [7]. The cyclic behaviour was then simulated in order to show the limitations of this kind of models when alternating compressive and tensile cycles. Figure 4 presents a comparison between the experimental data and the numerical predictions after 3 cycles for Al 2624 T351. Although the first cycle was accurately calibrated, the predicted responses for additional cycles show a clear overestimation in the yield stress. Similar results for Al 2624 T39 are presented in figure 5.

Table 1: Calibrated parameters of the isotropic hardening model

PARAMETER	**Al 2624 T351**	**Al 2624 T39**
$\boldsymbol{\sigma_0}$ [MPa]	360	434
$\boldsymbol{K}$ [MPa]	359	459
$\boldsymbol{n}$ [-]	0.42	0.61

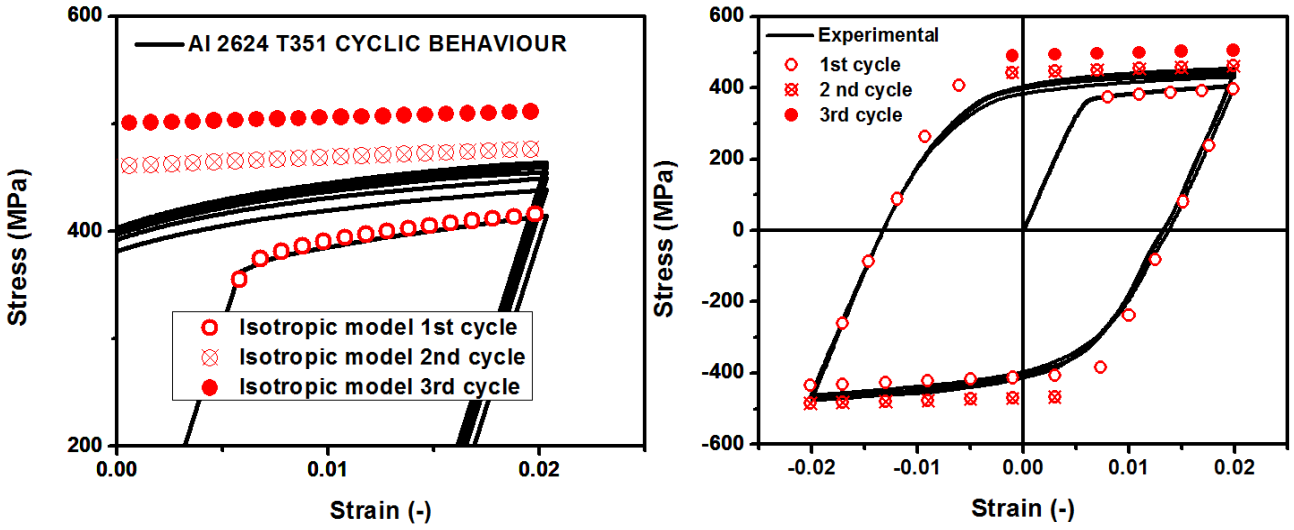

Figure 4: Comparison of cyclic experimental data with numerical predictions of the calibrated isotropic hardening model after 3 cycles in Al 2624 T351

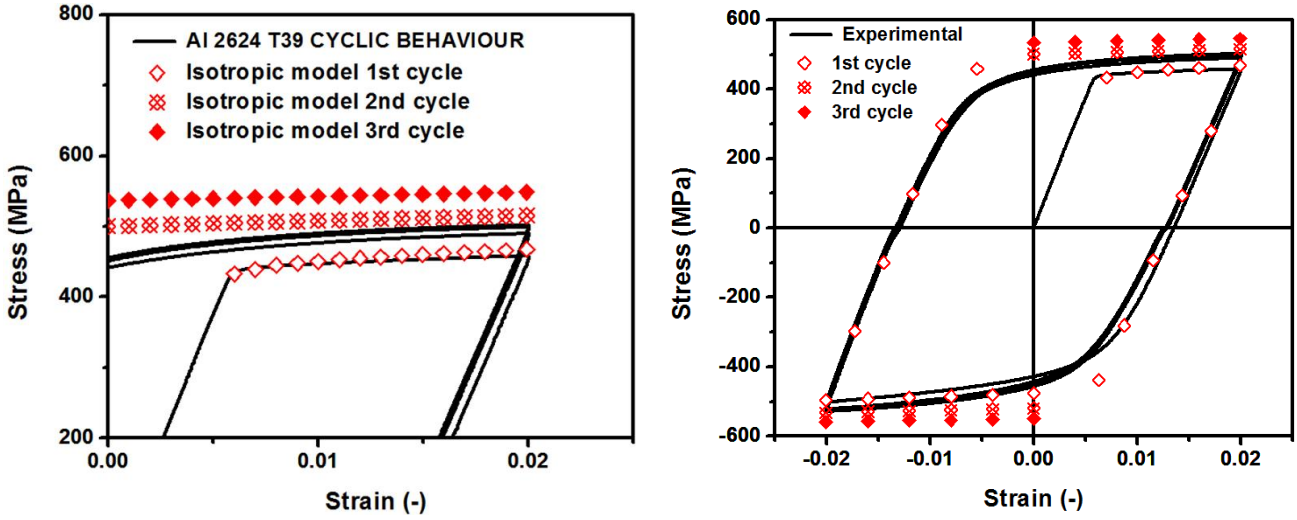

Figure 5: Comparison of cyclic experimental data with numerical predictions of the calibrated isotropic hardening model after 3 cycles in Al 2624 T39.

2.2.2 Combined isotropic + kinematic hardening model

In the combined hardening model, the isotropic behaviour is defined by Voce's formula (equation 12) [29] and the displacement of the yield stress is defined by Chaboche's kinematic hardening law (equation 13) [15]. Although advanced models have been developed to account for the multiaxial ratcheting behaviour of materials subject to multiple strain ranges, Chaboche's kinematic hardening law is able to predict the cyclic behaviour of the considered materials under symmetric tensile-compressive strain cycles.

Considering that the evolution of the back-stress is different depending on the cycle number and the evolution of the stress (tensile or compressive), equation 13 is particularized for every cycle in equations 14 to 17. The displacement of the yield surface during the first tensile cycle (from $\varepsilon = 0$ to $\varepsilon = 0.02$) is defined by equation 13. The first reverse yielding (from $\varepsilon = 0.02$ to $\varepsilon = -0.02$) is defined by equation 14. The second and third cycles are described by equations 15, 16 and 17. After the third cycle, the cyclic behaviour of the displacement of the yield surface is stabilized and equations 16 and 17 are applied for further cycles (equations 18 and 19). Constants E_i, F_i, G_i and H_i are calibrated to ensure the continuity of the displacement function.

$$\sigma_y(\Delta\varepsilon_p) = \sigma_0 + Q\left(1 - exp(-b\Delta\varepsilon_p)\right) \tag{12}$$

$$\alpha_{FY1}(\varepsilon_p) = \sum_{i=1}^{n} \frac{C_i}{\gamma_i}\left(1 - exp(-\gamma_i\varepsilon_p)\right) \tag{13}$$

$$\alpha_{RY1}(\varepsilon_p) = \sum_{i=1}^{n}\left(-\frac{C_i}{\gamma_i}\left(1 - exp(\gamma_i(\varepsilon_p + E_i))\right)\right) \tag{14}$$

$$\alpha_{FY2}(\varepsilon_p) = \sum_{i=1}^{n}\left(\frac{C_i}{\gamma_i}(1 - exp\left(-\gamma_i(\varepsilon_p + F_i)\right)\right) \tag{15}$$

$$\alpha_{RY2}(\varepsilon_p) = \sum_{i=1}^{n} -\frac{C_i}{\gamma_i}(1 - exp(\gamma_i(\varepsilon_p + G_i))) \tag{16}$$

$$\alpha_{FY3}(\varepsilon_p) = \sum_{i=1}^{n} \frac{C_i}{\gamma_i}\left(1 - exp\left(-\gamma_i(\varepsilon_p + H_i)\right)\right) \tag{17}$$

$$\alpha_{FYN}(\varepsilon_p) = \alpha_{FY3}(\varepsilon_p) \tag{18}$$

$$\alpha_{RYN}(\varepsilon_p) = \alpha_{RY2}(\varepsilon_p) \quad (19)$$

where:

$\alpha_{FYj}(\varepsilon_p)$ ≡ Front yielding displacement function for the "jth" cycle.

$\alpha_{RYj}(\varepsilon_p)$ ≡ Reverse yielding displacement function for the "jth" cycle.

As a criterion for a first approach to the best fit option, the stress at the end of the first half cycle (σ_{HC}), second (σ_2), third (σ_3) and the ultimate tensile strength (UTS) have been extracted from the experimental results and correlated with the isotropic and shift laws of the model (equations 20 to 23). Then, a least square method has been used to reach the final best fit option. The experimental data nearby the transition from tensile to compressive and vice versa has been neglected for the model calibration. This ensures better curve fitting for plastic strains close to the maximum and minimum strain ($\varepsilon_{max} = 0.02$ and $\varepsilon_{min} = -0.02$). Thus, better precision is expected in LSP conditions.

Regarding to the kinematic hardening parameters, (C_n, γ_n), unique pair of them have been used to define the yield surface displacement, (C_1, γ_1) since the precision achieved is enough in these particular alloys. However, multiple parameters $(C_1, \dots, C_n, \gamma_1, \dots, \gamma_n)$ could be used if necessary.

$$\sigma_{HC} = \sigma_y(\varepsilon_{PHC}) + \alpha_{FY1}(\varepsilon_{PHC}) = \sigma_0 + Q\left(1 - exp(-b\varepsilon_{PHC})\right) + \sum_{i=1}^{n} \frac{C_i}{\gamma_i}\left(1 - exp(-\gamma_i \varepsilon_{PHC})\right) \quad (20)$$

$$\sigma_2 = \sigma_y(5\varepsilon_{PHC}) + \alpha_{FY2}(\varepsilon_{PHC}) = \sigma_0 + Q\left(1 - exp(-5b\varepsilon_{PHC})\right) + \sum_{i=1}^{n} \frac{C_i}{\gamma_i}\left(1 - exp(-\gamma_i \varepsilon_{PHC})\right) \quad (21)$$

$$\sigma_3 = \sigma_y(9\varepsilon_{PHC}) + \alpha_{FY3}(\varepsilon_{PHC}) = \sigma_0 + Q\left(1 - exp(-9b\varepsilon_{PHC})\right) + \sum_{i=1}^{n} \frac{C_i}{\gamma_i}\left(1 - exp(-\gamma_i \varepsilon_{PHC})\right) \quad (22)$$

$$UTS = \sigma_0 + Q + \sum_{i=1}^{n} \frac{C_i}{\gamma_i} \quad (23)$$

In figures 6 and 7, the comparison between the experimental cyclic data and the numerical predictions of the combined hardening for Al 2624 T351 and Al 2624 T39 are represented respectively. Table 2 shows the fitting parameters used and the calibrated results. As is shown in the figures, the combined isotropic-kinematic hardening model developed in this section correlates well to the published experimental results for both material systems.

Table 2: Calibrated parameters of combined hardening models for Al 2624 T351 and Al 2624 T39

PARAMETER	Al 2624 T351	Al 2624 T39
$\boldsymbol{\sigma_1}$ [MPa]	398	458
$\boldsymbol{\sigma_2}$ [MPa]	430	488
$\boldsymbol{\sigma_3}$ [MPa]	443	500
$\boldsymbol{UTS}$ [MPa]	535	550
$\boldsymbol{Q}$ [MPa]	67	63
$\boldsymbol{b}$ [-]	15	17
$\boldsymbol{C_1}$ [MPa]	1844	1352
$\boldsymbol{\gamma_1}$ [-]	17	24

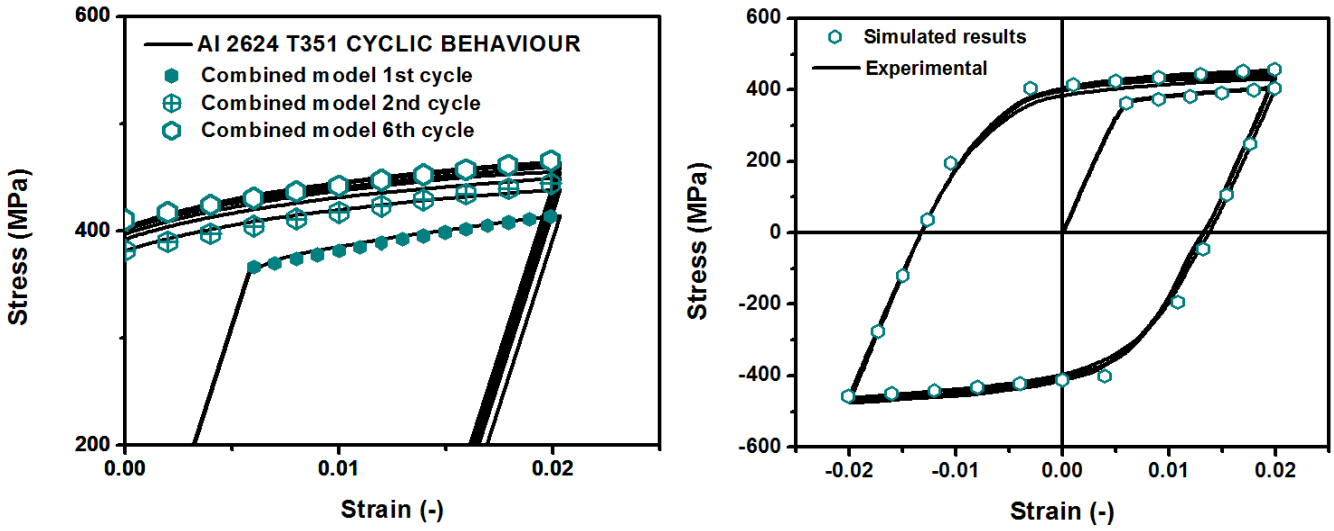

Figure 6: Comparison of cyclic experimental data with numerical predictions of the calibrated combined hardening model after 6 cycles in Al 2624 T351

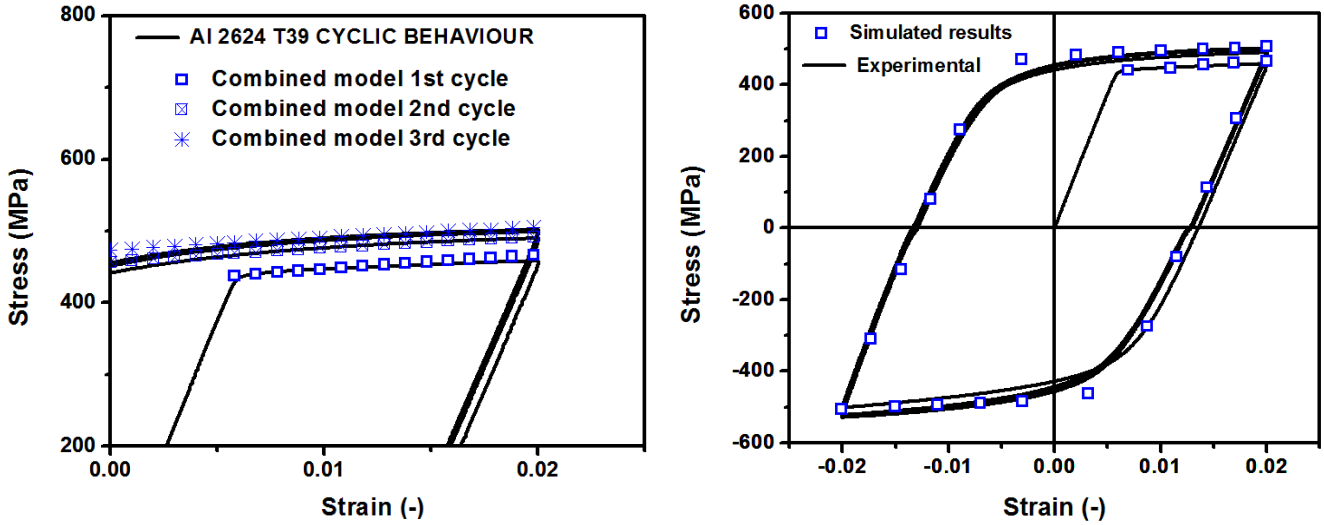

Figure 7: Comparison of cyclic experimental data with numerical predictions of the calibrated combined hardening model after 3 cycles in Al 2624 T39

3. Numerical simulation of LSP treatments with explicit consideration of cyclic deformation properties.

3.1. Simplified modelling of spatially coincident LSP pulses

In this section, a simplified modelling of spatially coincident LSP pulses is presented. Since the residual stresses are induced by the propagation of a shockwave through the material, each laser pulse is modelled as an incident spatial-temporal profile pressure pulse. Characteristic spatial-temporal dependences of the applied LSP pulses are taken from a previous work by the authors [4] and considered as typically representative (except possibly in the late part of plasma expansion, which is particularly difficult to assess) of the experimental LSP processes used in section 4.2 for validation of the developed model. The spatial distribution of the pressure pulse in cylindrical coordinates is presented in equation 24, where $a_{\emptyset}$ is a calibrated parameter for a $\emptyset = 2.50$ mm laser spot diameter. The temporal pressure pulse profile is represented in figure 8, in which the Hugoniot elastic limit of both alloys is shown.

$$P_0(t,\rho) = \begin{cases} P_0(\mathrm{t})exp\left(-a_{\emptyset}\dfrac{\rho^2}{(\emptyset/2)^2}\right), & \rho^2 < (\emptyset/2)^2 \\ 0 \quad , & \rho^2 \geq (\emptyset/2)^2 \end{cases} \tag{24}$$

where:

$$a_{\emptyset} = 0.85 \qquad for \qquad \emptyset = 2.50\ mm$$

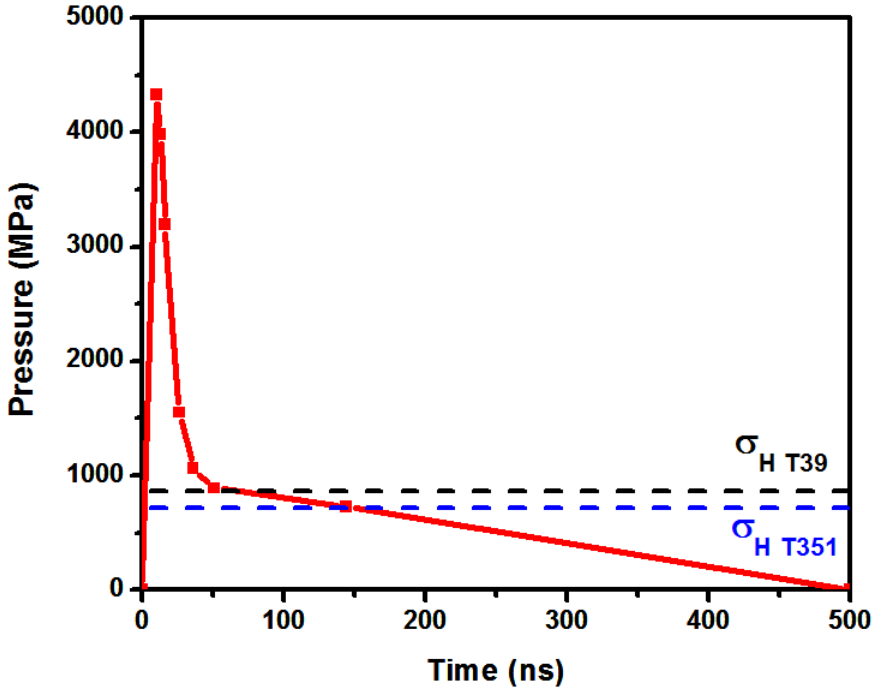

Figure 8: Temporal pressure pulse profile

Although fully 3D models are normally necessary to simulate realistic LSP treatments in which extended surfaces are involved, numerical predictions of spatially coincident LSP pulses are appropriate for checking the material behaviour under cyclic load-unload conditions. This scenario can be modelled using an axisymmetric formulation, which reduces the computation time significantly as compared to complete 3D simulations.

For this analysis, the element type used was CAX4R, which is a 4-node bilinear axisymmetric quadrilateral element with reduced integration and hourglass control. The dimensions of the optimized elements were 20 μm in the axial direction and 100 μm in the transverse direction. Both dimensions were optimized in order to ensure convergence, stability, and accuracy of the results. All simulations were performed using the SHOCKLAS calculation system, developed by the authors [4, 30, 31]. Considering that the time increment needed to model the temporal pressure pulse profile is in the order of nanoseconds, an explicit algorithm is used to simulate the application of the pressure pulses with the aid of the ABAQUS/explicit software [32].

In figures 9 and 10 the numerically predicted evolution of the deviatoric stress (defined as $-(\sigma_z - \sigma_r) = \sigma_r - \sigma_z$)) with respect to the axial total strain at the materials surface during the application of five successive pulses is represented for both the isotropic and combined isotropic + kinematic models for the cases of Al 2624 T351 and Al 2624 T39, respectively. While the isotropic model predicts an increase in the yield surface size during the plastic load and unload phenomenon with no saturation limit predicted, the consideration of the cyclic plasticity modelling though the combined model leads to an essentially correct saturation of the deviatoric stress.

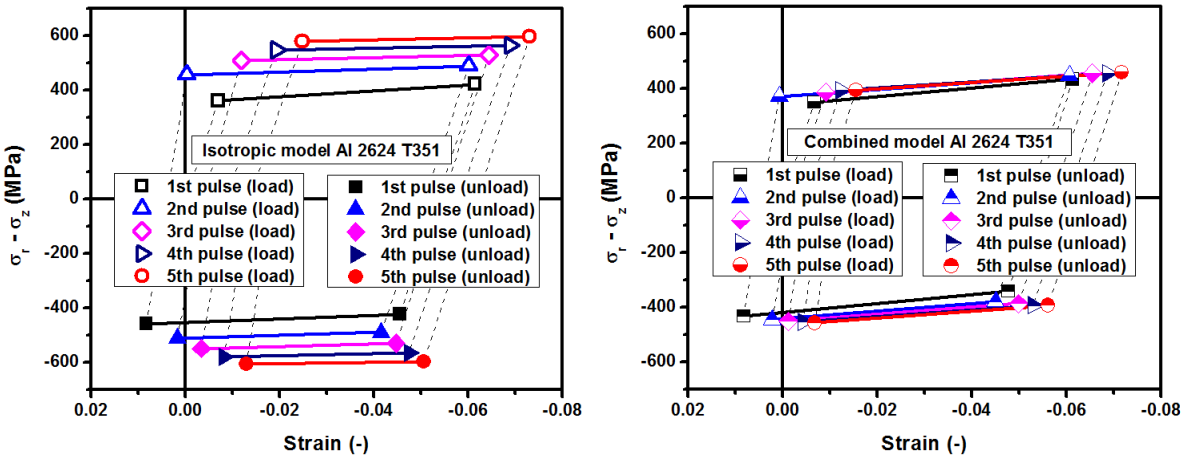

Figure 9: Deviatoric stress predicted for Al 2624 T351 at materials surface. Isotropic (left). Combined (right).

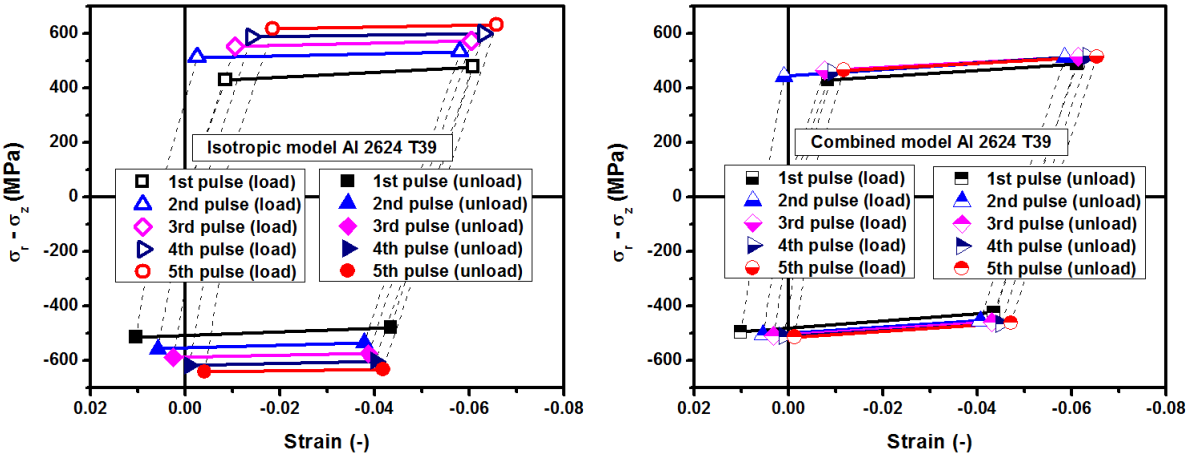

Figure 10: Deviatoric stress predicted for Al 2624 T39 at materials surface. Isotropic (left). Combined (right).

3.2. Estimation of a Representative Parameter of Cyclic Hardening Behaviour

As discussed previously, reverse yielding during LSP occurs only when the maximum applied pressure exceeds $2\sigma_H$. Once the laser-induced pulse pressure is applied to the material surface, a shockwave which amplitude at surface is P_{MAX} starts to propagate through the material. Following the work of Ballard *et al.*, [25], which assumes an elastic-perfectly plastic model, constant values of the elastic and plastic sound speed, c_e and c_p, respectively, and a triangular pressure pulse temporal profile, analytical estimations of the shockwave evolution as it propagates through the material can be formulated.

Initially the wave has sufficient intensity and energy to induce plasticity, and travels with speed c_p. As the laser-induced pulse pressure is extinguished and the energy of the pressure pulse dissipates, a load release elastic wave with speed c_e (c_e>c_p) propagates, reaching the plastic wave at a critical depth L_1 (equation 25). Successive reflections of the elastic release against the plastically compressed front wave suggest that, for depth values between L_1 and $2L_1$, the shockwave amplitude can be approximated as $P_{MAX} - 2\sigma_H$; for depths between $2L_1$ and $3L_1$ the shockwave amplitude would be $P_{MAX} - 4\sigma_H$, and so forth. Once the shockwave amplitude is σ_H, it becomes a purely elastic wave that propagates with speed c_e and the material experiences only elastic deformation at further depths. On this basis, the maximum pressure applied on the surface can be correlated with the in-depth pressure evolution of the shockwave (equation 26). Two characteristic

parameters can be extracted from the presented equations: The first one is the critical depth (L_c) which is defined as the affected depth in which the shockwave amplitude is twice the initial Hugoniot elastic limit (equation 27). The second one is the plastically affected depth (L_p), defined as the depth in which the shockwave amplitude is equal to the Hugoniot elastic limit (equation 28). While the critical depth describes a limit to the effect of reverse yielding, the plastically affected depth establishes a limit beyond which no residual stresses are achieved.

$$L_1 = \frac{c_e c_p}{c_e - c_p}\tau \tag{25}$$

$$\sigma_z(L_z) = Max\left(P_{MAX} - 2\sigma_H int\left(\frac{L_z}{L_1}\right), \sigma_H\right) \tag{26}$$

$$L_c = L_1\left(\frac{P_{MAX} - 2\sigma_H}{2\sigma_H}\right) \tag{27}$$

$$L_p = L_1\left(\frac{P_{MAX} - \sigma_H}{2\sigma_H}\right) \tag{28}$$

where:

L_z ≡ Distance from a point in the material to the surface.

$int\left(\frac{L_z}{L_1}\right)$ ≡ Integer part of $\frac{L_z}{L_1}$

τ ≡ Laser Pulse Duration (FWHM; Assumed triangular profile)

$c_e = \sqrt{\frac{E(1-\nu)}{\rho(1+\nu)(1-2\nu)}}$ Elastic wave speed (29)

$c_p = \sqrt{\frac{E}{3\rho(1-2\nu)}}$ Plastic wave speed (30)

These analytic results lead to a first approach to the shockwave evolution as it propagates through the material, but some limitations in the corresponding analytical predictions have to be considered, namely:

- The temporal pressure pulse profile used by Ballard *et al*. is considered to be triangular, while, in the realistic LSP case, the pressure on the solid target is partially maintained for a comparatively long time (almost 500 ns after the pulse launching) due to the inertia in dissipation of the plasma beneath the confining medium (water). This leads to an underestimation of the plastically affected depth by the simplified model.
- In the simplified model, the material density is considered to be constant, so that the elastic and plastic wave speeds are considered to remain constant as they propagate through the material. This, in turn leads to a lack of accuracy in the plastically affected depth estimation by the simplified model.
- An elastic-perfectly plastic model is considered, in which the Hugoniot elastic limit remains unaltered during plastic straining, which is not realistic since the yield surface size increases due to isotropic expansion. Hence, the analytic method offers a first approach to estimate the wave propagation only in the first cycle.

To address the limitations of the simplified analytical predictions, a more realistic shockwave in-depth evolution can be obtained with the aid of FEM simulations that incorporate the realistic evolution of the material properties (combined hardening model) and the realistic temporal pressure profile. The in-time shockwave evolution was obtained by means of FEM simulations for every single element. Figure 11 shows results for several significant depths. Therefore, the in-depth shockwave amplitude can be obtained and

compared with the simplified analytical results (figure 12 and table 3). This results are the most representative for the shockwave evolution considering that the material is subject to uniaxial strain behaviour (see section 2.1), which implies that the evolution of the three principal stresses is determined by the maximum pressure applied to each element (see figure 2). These results correspond to the application of the first pulse. Both the critical depth, L_c, and the plastically affected depth, L_p, are underestimated by the analytical predictions.

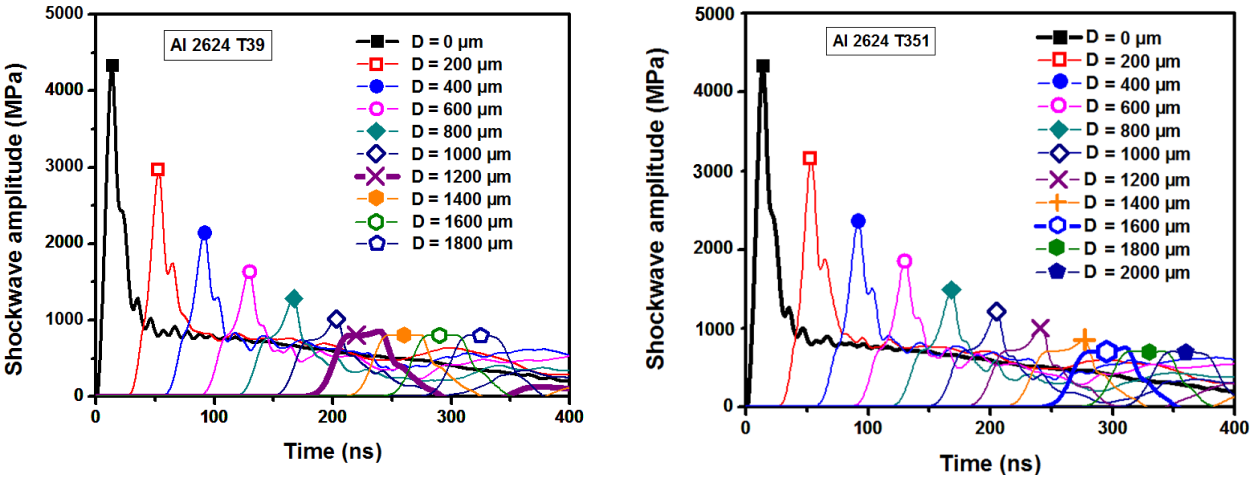

Figure 11: Realistic simulated in-time evolution of the shockwave for different significant depths in Al 2624 T39 (left) and Al 2624 T351 (right).

Regarding the shockwave evolution for the application of subsequent pulses, the aid of FEM simulations has been identified as essential considering that the material has already been deformed plastically in the previous cycles. Concretely, the critical depth and the plastically affected depth increase, which is not surprising since smaller amount of energy is dissipated in plastic straining as the wave propagates through the material.

The numerical predictions for the application of 1 to 5 pulses of L_{ci} and L_{pi} are presented in tables 4 and 5 respectively, in which slight differences are observed (less than 4%) depending on the hardening model. The combined hardening predictions are expected to be the correct ones as explicit consideration of cyclic properties have been taken into account. Thus, purely isotropic predictions lead only to an approximation of the critical depth and plastically affected depth. At this point, the combined hardening model estimations (the correct ones) of the critical and plastically affected depth will be named L_{ci} and L_{pi} respectively, where i represents the number of the pulse cycle.

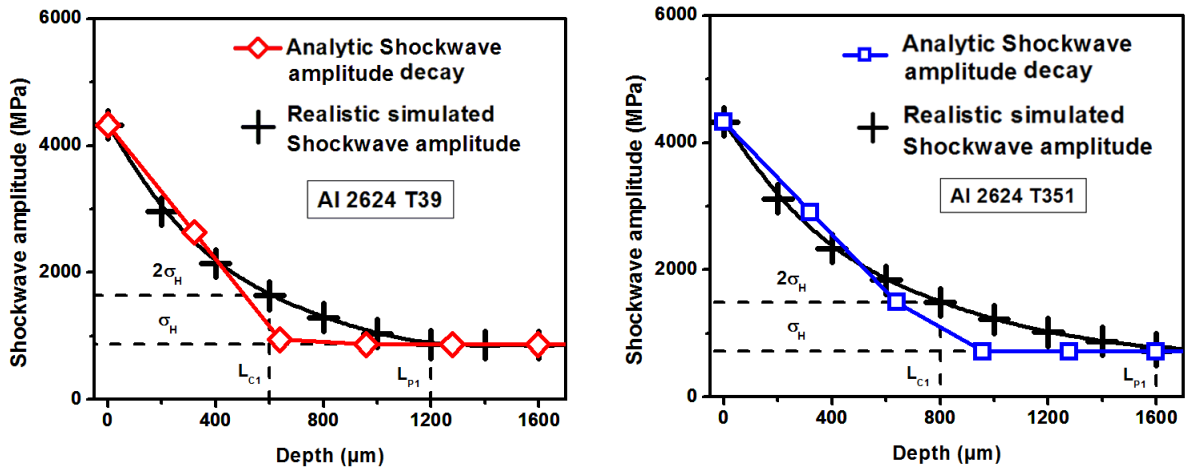

Figure 12: Realistic in-depth evolution of the shockwave amplitude for Al 2624 T39 (left) and Al 2624 T351 (right). As a reference, the simplified analytical predictions of the reference [25] are displayed.

Table 3: L_{ci} and L_{pi} parameters predicted for T39 and T351 alloys by the combined hardening model and corresponding simplified analytical values according to reference (Ballard et al., 1991).

MATERIAL	**Al 2624 T39**		**Al 2624 T351**	
Parameter	Analytical prediction	Combined model prediction	Analytical prediction	Combined model prediction
$\boldsymbol{L_{c1}}$ [µm]	493	600	676	800
$\boldsymbol{L_{p1}}$ [µm]	798	1200	957	1600

Table 4: L_{ci} parameter predicted for T39 and T351 alloys from 1 to 5 pulses with both models.

MATERIAL	**Al 2624 T39**		**Al 2624 T351**	
Parameter	Combined model prediction	Isotropic model prediction	Combined model prediction	Isotropic model prediction
$\boldsymbol{L_{c1}}$ [µm]	600	620	800	800
$\boldsymbol{L_{c2}}$ [µm]	720	700	900	900
$\boldsymbol{L_{c3}}$ [µm]	740	750	920	940
$\boldsymbol{L_{c4}}$ [µm]	770	790	940	960
$\boldsymbol{L_{c5}}$ [µm]	780	810	940	960

Table 5: L_{pi} parameter predicted for T39 and T351 alloys from 1 to 5 pulses with both models.

MATERIAL	**Al 2624 T39**		**Al 2624 T351**	
Parameter	Combined model prediction	Isotropic model prediction	Combined model prediction	Isotropic model prediction
$\boldsymbol{L_{p1}}$ [µm]	1200	1240	1600	1580
$\boldsymbol{L_{p2}}$ [µm]	1500	1460	1660	1640
$\boldsymbol{L_{p3}}$ [µm]	1780	1760	1720	1740
$\boldsymbol{L_{p4}}$ [µm]	1840	1860	1840	1820
$\boldsymbol{L_{p5}}$ [µm]	1900	1920	2000	2000

From these results, and considering that cyclic plasticity is only present for shockwave amplitudes above $2\sigma_H$, two different regions can been identified along the in-depth profile. These regions are delimited by the critical depth, L_{ci}, (estimated by the combined hardening model) and are defined as follows:

i) From the material surface to L_{ci}, the shockwave amplitude is above $2\sigma_H$. Thus, reverse yielding is present and different results are expected between the combined and isotropic hardening models. As presented in the results section, lower compressive residual stresses are predicted by the combined hardening model.

ii) Beyond the estimated critical depth L_{ci} the shockwave amplitude is less than twice the Hugoniot elastic limit ($\sigma_z(L_z) < 2\sigma_H$). Thus, no reverse yielding is present and both models tend to converge to the same residual stress predictions.

Consequently, L_{ci} is a critical parameter to represent the material limiting depth for which cyclic plasticity effects are expected. Obviously, considering that the constitutive equations of the isotropic and combined models presented in this paper are essentially different, slight differences are observed beyond the estimated critical depth.

In a similar way, the plastically affected depth L_{pi}, also underestimated by the simplified model, is considered to be a very useful parameter for the recursive estimation of the practical depth for which the plastic effect of successive pulses on the material induce plastic deformation (as shown in the next section).

4. Results and discussion

4.1. Residual stress profiles after the application of successive concentric pressure pulses

In this section the residual stresses predicted using the developed combined hardening model are compared to results based on a conventional isotropic hardening model (Johnson-Cook model) through the numerical FEM simulation of spatially coincident LSP pulses. The residual stress profiles corresponding to the application of 1 and 5 concentric pulses with 4.33 GPa peak pressure are displayed in figures 13 and 14, showing the effect on the combined material model of the cyclic plasticity. On one hand, the results clearly confirm the analytical predictions formulated through consideration of the peak pressure decay presented in section 3.2: from the surface to the estimated critical depth (L_{ci}), the shockwave amplitude is above $2\sigma_H$ and clear differences are observed between the isotropic and combined hardening models. Specifically, lower (in absolute value) compressive residual stresses are predicted by the combined hardening model, which is consistent with the results presented previously in figures 9 and 10. Beyond the estimated critical depth (L_{ci}) and until the plastically affected depth (L_{pi}), both curves tend to converge to the same residual stress predictions. The slight differences observed from the estimated critical depth (L_{ci}) to the plastically affected depth (L_{pi}) may be motivated by the fact that the constitutive equations of both models are essentially different, which has already been discussed in the previous section.

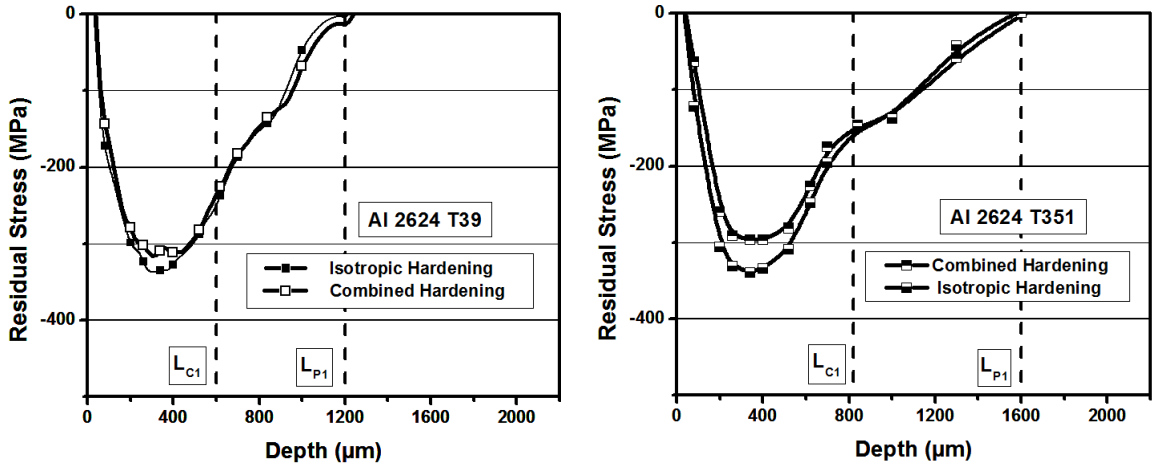

Figure 13: Residual stress profile after the application of one pressure pulse with peak of 4.33 GPa. Comparison between the results predicted for Al 2624 T39 (left) and Al 2624 T351 (right).

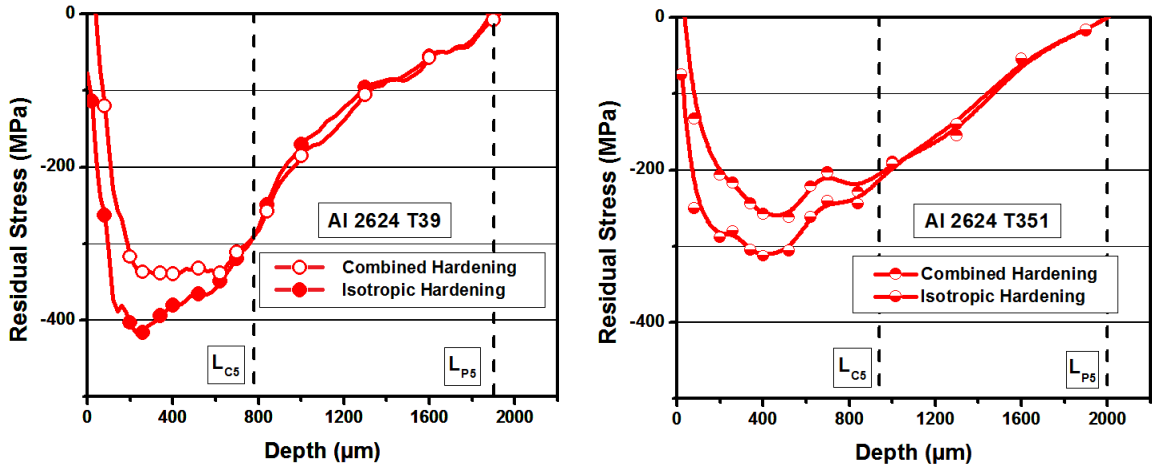

Figure 14: Residual stress profile after the application of five pressure pulses with peak of 4.33 GPa. Comparison between the results predicted for Al 2624 T39 (left) and Al 2624 T351 (right).

4.2. Realistic modelling of Extended Surface High-Coverage LSP Treatments

The effect of cyclic plasticity modelling in the calculated residual stresses has been demonstrated with the aid of the low-computational-cost axisymmetric model. The next step is to study realistic cases in which extended surfaces are affected by LSP treatments. In this section, the results corresponding to two different treatments applied to the Al 2624 T39 alloy are calculated under a fully 3D FEM approach of the SHOCKLAS calculation system including, in one case, a purely isotropic Johnson-Cook material model (taken as reference) and, for the other case, the developed combined isotropic + kinematic material model. A detailed description of both simulated treatments is presented in table 6, showing the laser spot diameter, the peak intensity and the equivalent overlapping density (EOD), which is defined as the number of applied pulses per cm^{-2} [33]. The specimen subject to treatment is a plate whose thickness is 12.7 mm and the treated surface is a squared area of 900 mm^2.

Table 6: Low and high density treatments description.

TREATMENT	Laser spot Ø [mm]	Peak Intensity [GW cm^{-2}]	EOD [pulses cm^{-2}]
1 (Low density)	2.5	10.4	278
2 (High density)	2.5	10.4	625

A comparison between the obtained numerical predictions and the experimental results also obtained by the authors for the corresponding extended LSP treatments is presented in figures 15 and 16. The experimental results have been obtained by means of the hole drilling method, in which material is drilled and the resulting deformation as the material is removed is measured by a precision strain gage, which is finally converted to residual stress with the aid of a specific algorithm. Consequently, the FEM numerical predictions have been extracted and averaged from a representative squared area similar to the material removed by the hole drilling method. Once this area is above 1 mm^2, simulated results converge to the ones presented in figures 15 and 16 independently of the position of the treated area. The observed results are as expected after the discussions in previous sections: the simulations using the developed combined model predict a saturation value in the finally achieved residual stress fields up to a certain depth that can be correlated to the final position of the critical depth after repeated overlapped pulses. In contrast, the simulations using the reference isotropic hardening model predict an unbounded increase in the residual stresses between two treatments studied (Table 6), which is not consistent with the experimentally determined stress-strain properties of the material or the experimentally measured residual stresses. This limited increase in the residual stresses for high density treatments has been documented [34] and cannot be predicted by isotropic models. This overestimation is expected to be more obvious for higher density treatments (*i.e.*, even higher than those considered in the present article).

As shown in figure 16, a better agreement between the FEM predictions and experimental results is obtained for the high density treatment modelled using combined hardening. This can be a result of uncertainties resulting from the inherent geometrical complexity involved in partially overlapped pressure pulses in the low density treatment. However, even with the consideration of the possible uncertainties associated with the experimental method used to measure the residual stress profiles (hole drilling method; see reference [34], the use of the combined isotropic + kinematic hardening model is able to readily predict both the saturation effect referred in the previous paragraph and the general depth profile of the residual stresses, especially at the material surface, while the purely isotropic model predicts unacceptably high compressive residual stresses that are not observed experimentally.

While this comparative result clearly indicates the inappropriateness of the use of purely isotropic hardening models in the comprehensive simulation of LSP treatments and the general appropriateness of combined isotropic + kinematic hardening models to represent a more realistic behaviour of ductile materials under cyclic load, model improvements are required to improve the global agreement of the numerically predicted results. This is especially true for experimental data at depths on the order of the estimated critical depth and, also for depths in the range from the critical depth, L_{ci}, to the plastically affected depth, L_{pi}.

The discrepancies between simulation predictions and experimental results are in part a consequence of the comparatively prolonged time during which the confining medium (water in the case of the reported experiments) causes a peak plasma pressure exceeding the Hugoniot elastic limit, σ_H, and, thus, continues to induce plastic (although not cyclic plastic) deformation of the material. The models presently used by the authors for the estimation of the spatial-temporal profile of the pressure pulse applied to the LSP treated material have been subject of intense development [30], but still present some uncertainties in the late part of the temporal profile of the pressure pulse, precisely in the sense that can directly affect the induction of plastic deformation in the lower plasticity regime, *i.e.*, the region close to the plastically affected depth.

The development of new knowledge around the plasma expansion simulation models (ultimately determining the true pressure applied to the treated material) is the subject of present investigations by the authors and is likely to provide more precise spatial-temporal profiles allowing a better prediction of the overall realistic geometry simulation results to experimental determinations.

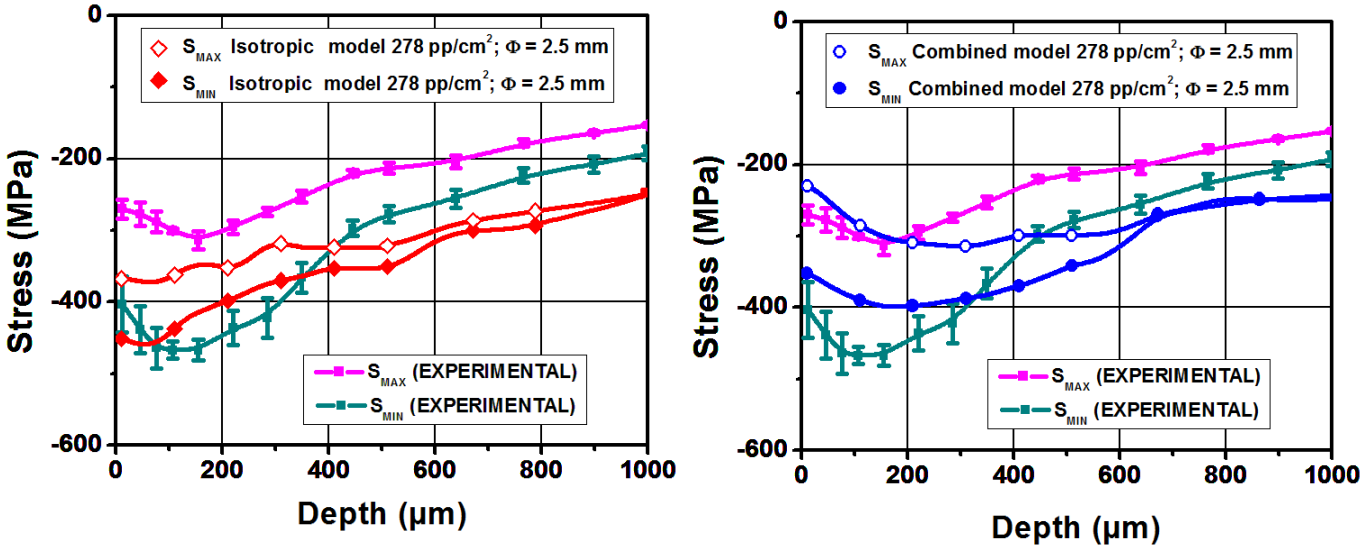

Figure 15: Experimental results vs numerical predictions for low density treatment. Isotropic model predictions (left) vs combined ones (right)

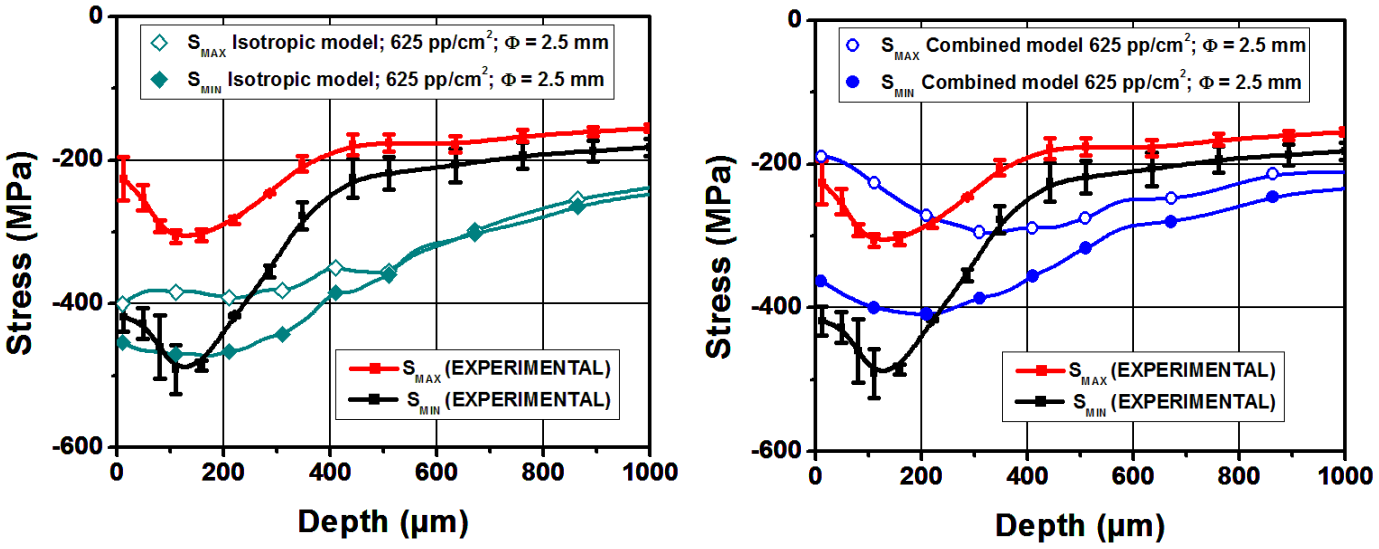

Figure 16: Experimental results vs numerical predictions for high density treatment. Isotropic model predictions (left) vs combined ones (right)

5. Conclusions

The cyclic plasticity behaviour during laser shock processing (LSP) has a significant influence on the residual stresses as corroborated by numerical calculation. Despite intuitive arguments suggesting that only compressive yielding is involved, the analysis of the physical basis of materials deformation in this case leads to the identification of a plastic recovery when the applied pressures exceed twice the Hugoniot elastic limit, which is frequently the case in LSP processes. The depth affected by cyclic plasticity has been determined as a critical parameter for the choice of a suitable material deformation model.

On the basis of experimental cyclic stress-strain data, a combined isotropic + kinematic hardening model has been developed that can realistically reproduce the cyclic deformations in material subject to alternating tensile-compressive cycles, overcoming the errors inherent in applying purely isotropic hardening models.
The application of the developed combined hardening model to the numerical simulation of fully overlapped LSP pulses in Al 2624 T351 and Al 2624 T39 has confirmed the theoretical predictions. In addition, in the case of extended surface high-coverage LSP treatments, better agreement with the experimental results is predicted by the combined hardening model.

The overall conclusions are detailed as follows:

i) Numerical predictions of the residual stress distributions in the treated material are affected by cyclic plasticity in near-surface regions where the shockwave amplitude propagating through the material exceeds twice the Hugoniot elastic limit ($P > 2\sigma_{\mathrm{H}}$). For greater depths, no cyclic plasticity effect is to be expected.

ii) Correspondingly, material hardening models that incorporate cyclic plasticity effects associated with the Bauschinger effect must be taken into account for accurate prediction of residual stress fields induced by laser shock processing. Purely isotropic hardening models essentially predict higher compressive residual stresses from the surface to the referred critical depth (L_{ci}) in which the peak shockwave amplitude is equal to twice the Hugoniot elastic limit.

iii) The combined isotropic + kinematic hardening model presented in this article provides a practical solution for the proper modelling of cyclic plasticity processes and the presented methodology for its material calibration is considered as a direct and conceptually sound procedure for application to any material of interest. This results in an improved capability to design a proper LSP treatment.

iv) The effect of cyclic plasticity modelling in extended surface high-coverage LSP treatments has been demonstrated: while isotropic hardening models overestimate the residual stresses, a better agreement with the experimental results is obtained by the combined hardening models.

Although the benefits of combined isotropic + kinematic hardening models for predicting LSP-induced residual stresses via FEM have been fully demonstrated, there exists a need for improvement in the prescription of the input data for simulations (not affecting to the material models themselves). This need was observed in the present study through consideration of the critical depth and the plastically affected depth as key parameters for the analysis of the cyclic plastic behaviour. Additionally, material damage models consistent with the developed model are envisaged as future development targets.

Acknowledgements

This research effort was sponsored by the Air Force Office of Scientific Research, Air Force Material Command, USAF, under grant number FA9550-14-1-0415, and the Air Force Research Laboratory's Aerospace Vehicles Directorate. The U.S. Government is authorized to reproduce and distribute reprints for Government purpose notwithstanding any copyright notation thereon. The views and conclusions contained herein are those of the authors and should not be interpreted as necessarily representing the official policies or endorsements, either expressed or implied, of the Air Force Office of Scientific Research or the U.S. Government. The authors would like to thank Dr Markus Heinimann at Alcoa Inc. (now Arconic) for the provision of the material studied in the project. MEF is grateful for funding from the Lloyd's Register

Foundation, a charitable foundation helping to protect life and property by supporting engineering-related education, public engagement and the application of research.

Work partly supported by MINECO (Spain; Project MAT2015-63974-C4-2-R).

References

[1] Correa C, Gil-Santos A, Porro J.A., Díaz M., Ocaña J.L., Eigenstrain simulation of residual stresses induced by laser shock processing in a Ti6Al4V hip replacement. Materials & Design, 79 (2015), pp. 106-114. https://doi.org/10.1016/j.matdes.2015.04.048

[2] Zhang X.Q., Li H., Yu X.L., Zhou Y., Duan S.W., Li S.Z., Huang Z.L., Zuo L.S., Investigation on effect of laser shock processing on fatigue crack initiation and its growth in aluminum alloy plate. Materials & Design, 65 (2015), pp. 425-431. https://doi.org/10.1016/j.matdes.2014.09.001

[3] Zhang L., Lu J.Z., Zhang Y.K., Luo K.Y., Zhong J.W., Cui C.Y., Kong D.J., Guan H.B., Qian X.M., Effects of different shocked paths on fatigue property of 7050-T7451 aluminum alloy during two-sided laser shock processing, Materials & Design, 32 (2011), pp. 480-486. https://doi.org/10.1016/j.matdes.2010.08.039

[4] Correa C., de Lara L.R., Díaz M., Porro J.A., García-Beltrán A., Ocaña J.L., Influence of pulse sequence and edge material effect on fatigue life of Al2024-T351 specimens treated by laser shock processing, Int J Fatigue, 70 (2015), pp. 196-204

[5] Johnson, G.R., Cook, W.H., Fracture characteristics of three metals subjected to various strains, strain rates, temperatures and pressures. Engineering fracture mechanics, 21 (1985), pp. 31-48. https://doi.org/10.1016/0013-7944(85)90052-9

[6] Chun, B.K., Jinn, J.T., Lee, J.K., Modeling the Bauschinger effect for sheet metals, part I: theory. International Journal of Plasticity, 18 (2002), pp. 571-595. https://doi.org/10.1016/S0749-6419(01)00046-8

[7] Zabeen, S., Khan, M.K., Fitzpatrick, M.E., Mechanisms of residual stress generation in mechanical surface treatment: the role of cyclic plasticity and texture. Report EOARD AFRL-AFOSR-UK-TR-2015 (2015).

[8] Prager, W., A new methods of analyzing stresses and strains in work hardening plastic solids. ASME Journal of Applied Mechanics, 23 (1956), pp. 493-496.

[9] Besseling, J.F., A theory of elastic, plastic, and creep deformations of an initially isotropic material. ASME Journal of Applied Mechanics, 25 (1958), pp. 529-536.

[10] Dafalias, Y.F., Popov, E.P., A model of nonlinearly hardening materials for complex loading. Acta Mechanica, 21 (1975), pp. 173–192. https://doi.org/10.1007/BF01181053

[11] Dafalias, Y.F., Popov, E.P., Plastic internal variables formalism of cyclic plasticity. ASME Journal of Applied Mechanics, 43 (1976), pp. 645–651. https://doi:10.1115/1.3423948

[12] Krieg, R.D., A practical two-surface plasticity theory. ASME Journal of Applied Mechanics, 42 (1975), pp. 641–646. https://doi:10.1115/1.3423656

[13] Mroz, Z., On the description of anisotropic work hardening. Journal of Mechanics and Physics of Solids, 15 (1967), pp. 163–175. https://doi.org/10.1016/0022-5096(67)90030-0

[14] Armstrong, P.J., Frederick, C.O., A mathematical representation of the multiaxial Bauschinger effect. Central Electricity Generating Board [and] Berkeley Nuclear Laboratories, Research & Development Department, 731 (1966).

[15] Chaboche, J.L., Time-independent constitutive theories for cyclic plasticity. International Journal of Plasticity, 2 (1986), pp. 149–188. https://doi.org/10.1016/0749-6419(86)90010-0

[16] Chaboche, J.L., On some modifications of kinematic hardening to improve the description of ratcheting effects. International Journal of Plasticity, 7 (1991), pp. 661–678. https://doi.org/10.1016/0749-6419(91)90050-9

[17] Ohno, N., Wang, J.D., Kinematic hardening rules with critical state of dynamic recovery, part I: formulations and basic features for ratcheting behaviour. International Journal of Plasticity, 9 (1993), pp. 375–390. https://doi.org/10.1016/0749-6419(93)90042-O

[18] Abdelkarim, M., Ohno, N., Kinematic hardening model suitable for ratcheting with steady-state. International Journal of Plasticity, 16 (2000), pp. 225–240. https://doi.org/10.1016/S0749-6419(99)00052-2

[19] Bari, S., Hassan, T., An advancement in cyclic plasticity modeling for multiaxial ratcheting simulation. International Journal of Plasticity, 18 (2002), pp. 873– 894. https://doi.org/10.1016/S0749-6419(01)00012-2

[20] Chen, X., Jiao, R., Modified kinematic hardening rule for multiaxial ratcheting prediction. International Journal of Plasticity, 20 (2004), pp. 871–898. https://doi.org/10.1016/j.ijplas.2003.05.005

[21] Chen, X., Jiao, R., Kim, K.S., On the Ohno–Wang kinematic hardening rules for multiaxial ratcheting modeling of medium carbon steel. International Journal of Plasticity, 21 (2005), pp. 161–184. https://doi.org/10.1016/j.ijplas.2004.05.005

[22] Jiang, Y., Sehitoglu, H., Modeling of cyclic ratchetting plasticity, part I: development of constitutive relations. ASME Journal of Applied Mechanics, 63 (1996), pp. 720–725. https://doi:10.1115/1.2823355

[23] McDowell, D.L., Stress state dependence of cyclic ratcheting behaviour of two rail steels. International Journal of Plasticity, 11 (1995), pp. 397–421. https://doi.org/10.1016/S0749-6419(95)00005-4

[24] Voyiadjis, G.Z., Basuroychowdhury, I.N., A plasticity model for multiaxial cyclic loading and ratchetting. Acta Mechanica, 126 (1998), pp. 19–35. https://doi.org/10.1007/BF01172796

[25] Ballard, P., Fournier, J., Fabbro, R., Frelat, J., Residual stresses induced by laser-shocks. Le Journal de Physique IV, 1 (1991), pp. C3-487 - C3-494. https://doi.org/10.1051/jp4:1991369

[26] Morales, M., Ocaña, J.L., Molpeceres, C., Porro, J.A., García-Beltrán, A., Model based optimization criteria for the generation of deep compressive residual stress fields in high elastic limit metallic alloys by ns-laser shock processing. Surface and Coatings Technology, 202 (2008), pp. 2257-2262. https://doi.org/10.1016/j.surfcoat.2007.12.007

[27] Morales, M., Porro, J.A., Blasco, M., Molpeceres, C., Ocaña, J.L., Numerical simulation of plasma dynamics in laser shock processing experiments. Applied Surface Science, 255 (2009), pp. 5181-5185. https://doi.org/10.1016/j.apsusc.2008.09.067

[28] Peyre, P., Fabbro, R., Merrien, P., Lieurade, H.P., Laser shock processing of aluminium alloys. Application to high cycle fatigue behaviour. Materials Science and Engineering: A, 210 (1996), pp. 102-113. https://doi.org/10.1016/0921-5093(95)10084-9

[29] Voce, E., The relationship between stress and strain for homogeneous deformation. J. Inst. Metals, 74 (1948), pp. 62-537.

[30] Morales, M., Correa, C., Porro, J.A., Molpeceres, C., Ocaña, J.L., Thermomechanical modelling of stress fields in metallic targets subject to laser shock processing. International Journal of Structural Integrity, 2 (2011), pp. 51-61. https://10.4028/www.scientific.net/MSF.638-642.2682

[31] Ocaña, J.L., Morales, M., Molpeceres, C., Torres, J., Numerical simulation of surface deformation and residual stresses fields in laser shock processing experiments. Applied Surface Science, 238 (2004), pp. 242-248. https://doi.org/10.1016/j.apsusc.2004.05.232

[32] Hibbitt, Karlsson, Sorensen., ABAQUS/Explicit: user's manual. Hibbitt, Karlsson and Sorenson Incorporated; (2001).

[33] Ocaña, J.L., Porro, J.A , Morales, M., Iordachescu, D., Díaz, M., Ruiz De Lara, L., Correa, C., Gil-Santos, A., Laser shock processing: an emerging technique for the enhancement of surface properties and fatigue life of high-strength metal alloys. International Journal of Microstructure and Materials Properties, 8 (2013), pp. 38-52. https://doi.org/10.1504/IJMMP.2013.052645

[34] Ocaña, J.L., Molpeceres, C., Porro, J.A., Gómez, G., Morales, M., Experimental assessment of the influence of irradiation parameters on surface deformation and residual stresses in laser shock processed metallic alloys Applied Surface Science, 238 (2004b), pp. 501-505. https://doi.org/10.1016/j.apsusc.2004.05.246

Footnotes

-Figure 1: σ_z-ε_{pz} diagram for $P_{MAX}>2\sigma_H$.
-Figure 2: σ_z- σ_r diagram for $P_{MAX}>2\sigma_H$.
-Figure 3: Experimental results of strain-control cycles up to 7 cycles with a maximum strain of ±2%. T39 (left), T351 (right).
-Figure 4: Comparison of cyclic experimental data with numerical predictions of the calibrated isotropic hardening model after 3 cycles in Al 2624 T351
-Figure 5: Comparison of cyclic experimental data with numerical predictions of the calibrated isotropic hardening model after 3 cycles in Al 2624 T39.
-Figure 6: Comparison of cyclic experimental data with numerical predictions of the calibrated combined hardening model after 6 cycles in Al 2624 T351
-Figure 7: Comparison of cyclic experimental data with numerical predictions of the calibrated combined hardening model after 3 cycles in Al 2624 T39
-Figure 8: Temporal pressure pulse profile
-Figure 9: Deviatoric stress predicted for Al 2624 T351 at materials surface. Isotropic (left). Combined (right).
-Figure 10: Deviatoric stress predicted for Al 2624 T39 at materials surface. Isotropic (left). Combined (right).
-Figure 11: Realistic simulated in-time evolution of the shockwave for different significant depths in Al 2624 T39 (left) and Al 2624 T351 (right).
-Figure 12: Realistic in-depth evolution of the shockwave amplitude for Al 2624 T39 (left) and Al 2624 T351 (right). As a reference, the simplified analytical predictions of the reference [25] are displayed.
-Figure 13: Residual stress profile after the application of one pressure pulse with peak of 4.33 GPa. Comparison between the results predicted for Al 2624 T39 (left) and Al 2624 T351 (right).
-Figure 14: Residual stress profile after the application of five pressure pulses with peak of 4.33 GPa. Comparison between the results predicted for Al 2624 T39 (left) and Al 2624 T351 (right).
-Figure 15: Experimental results vs numerical predictions for low density treatment. Isotropic model predictions (left) vs combined ones (right)
-Figure 16: Experimental results vs numerical predictions for high density treatment. Isotropic model predictions (left) vs combined ones (right)

Tables

Table 1: Calibrated parameters of the isotropic hardening model

PARAMETER	**Al 2624 T351**	**Al 2624 T39**
$\boldsymbol{\sigma_0}$ [MPa]	360	434
$\boldsymbol{K}$ [MPa]	359	459
$\boldsymbol{n}$ [-]	0.42	0.61

Table 2: Calibrated parameters of combined hardening models for Al 2624 T351 and Al 2624 T39

PARAMETER	**Al 2624 T351**	**Al 2624 T39**
$\boldsymbol{\sigma_1}$ [MPa]	398	458
$\boldsymbol{\sigma_2}$ [MPa]	430	488
$\boldsymbol{\sigma_3}$ [MPa]	443	500
$\boldsymbol{UTS}$ [MPa]	535	550
Q [MPa]	67	63
b [-]	15	17
$\boldsymbol{C_1}$ [MPa]	1844	1352
$\boldsymbol{\gamma_1}$ [-]	17	24

Table 3: L_{ci} and L_{pi} parameters predicted for T39 and T351 alloys by the combined hardening model and corresponding simplified analytical values according to reference (Ballard et al., 1991).

MATERIAL	**Al 2624 T39**		**Al 2624 T351**	
Parameter	Analytical Prediction	Combined model prediction	Analytical Prediction	Combined model prediction
$\boldsymbol{L_{c1}}$ [µm]	493	600	676	800
$\boldsymbol{L_{p1}}$ [µm]	798	1200	957	1600

Table 4: L_{ci} parameter predicted for T39 and T351 alloys from 1 to 5 pulses with both models.

MATERIAL	**Al 2624 T39**		**Al 2624 T351**	
Parameter	Combined model prediction	Isotropic model prediction	Combined model prediction	Isotropic model prediction
$\boldsymbol{L_{c1}}$ [µm]	600	620	800	800
$\boldsymbol{L_{c2}}$ [µm]	720	700	900	900
$\boldsymbol{L_{c3}}$ [µm]	740	750	920	940
$\boldsymbol{L_{c4}}$ [µm]	770	790	940	960
$\boldsymbol{L_{c5}}$ [µm]	780	810	940	960

Table 5: L_{pi} parameter predicted for T39 and T351 alloys from 1 to 5 pulses with both models.

MATERIAL	**Al 2624 T39**		**Al 2624 T351**	
Parameter	Combined model prediction	Isotropic model prediction	Combined model prediction	Isotropic model prediction
$\boldsymbol{L_{p1}}$ [µm]	1200	1240	1600	1580
$\boldsymbol{L_{p2}}$ [µm]	1500	1460	1660	1640
$\boldsymbol{L_{p3}}$ [µm]	1780	1760	1720	1740
$\boldsymbol{L_{p4}}$ [µm]	1840	1860	1840	1820
$\boldsymbol{L_{p5}}$ [µm]	1900	1920	2000	2000

Table 6: Low and high density treatments description.

TREATMENT	**Laser spot Ø [mm]**	**Peak Intensity [GW cm^{-2}]**	**EOD [pulses cm^{-2}]**
1 (Low density)	2.5	10.4	278
2 (High density)	2.5	10.4	625